

Depth of Ellerman Burst Derived from High-resolution H α and Ca II 8542 A Spectra

Minju Seo¹, Carlos Quintero Noda², Jeongwoo Lee³, and Jongchul Chae¹ Department of Physics and Astronomy, Seoul National University, Seoul 08826, Republic of Korea ² Institute of Space and Astronautical Science, Japan Aerospace Exploration Agency, Sagamihara, Kanagawa 252-5210, Japan Institute of Space Sciences, Shandong University, Weihai, Shandong 264209, People's Republic of China; leej@sdu.edu.cn Received 2018 September 27; revised 2018 November 22; accepted 2018 November 30; published 2019 January 25

Abstract

High-resolution spectra of an Ellerman burst (EB) sampling the H α and the Ca II 8542 Å lines obtained with the Fast Imaging Solar Spectrograph (FISS) installed on the 1.6 m Goode Solar Telescope at the Big Bear Solar Observatory are compared with synthetic line profiles constructed using the RH code for nonlocal thermodynamical equilibrium radiative transfer. The EB heating is modeled by a local temperature hump above the quiet-Sun temperature. Our first finding is that FISS H α and Ca II 8542 Å intensity profiles cannot be reproduced simultaneously by a single hump model as far as the hump is thicker than ≥100 km. Simultaneous reproduction of both line profiles is possible when the EB temperature enhancement is confined to a layer as thin as \leq 20 km in the photosphere where the H α wing response is high and that of the Ca II 8542 Å is not. Moreover, when we examine the EB spectra at different times, we find that the EB at a time of weaker appearance is located at lower heights, \sim 50 km, and moves upward to \sim 120 km at the time of maximum intensity. Complementary calculations of the Na I D₁ and Mg I b₂ lines as well as that of UV continuum at 1600 and 1700 Å with the deduced EB atmosphere are also performed to test the result, which allows us to discuss the shortcomings of this plane parallel static model atmosphere for understanding the physical properties of EBs.

Key words: line: formation – line: profiles – Sun: activity – Sun: atmosphere – Sun: chromosphere – Sun: photosphere

1. Introduction

Ellerman bursts (EBs) are small transient events that appear as an intensity brightening on the far wings of the H α spectral line (Ellerman 1917). EBs are observed in the vicinity of active regions, and they have a size of about 1" and a lifetime shorter than 30 minutes (Nelson et al. 2013; Rutten et al. 2013). Besides the hydrogen Balmer series, EBs are also detected at additional wavelengths such as the continuum at 1600 A (Qiu et al. 2000) and 1700 Å (Vissers et al. 2013), the He I D3 and 10830 Å lines (Libbrecht et al. 2017), the Ca II H and K (Matsumoto et al. 2008) lines, and the Ca II 8542 Å (Fang et al. 2006; Yang et al. 2013) line. At the same time, EBs leave no trace on the Na I D and Mg I b lines as noted by Ellerman and confirmed by Rutten et al. (2015). In the case of the EUV spectrum, EBs are detected both in the Mg II h and k lines and in the Si IV line (Vissers et al. 2015; Grubecka et al. 2016). EBs have been commonly believed to be due to magnetic reconnection (e.g., Vissers et al. 2013) located in the lower chromosphere (Georgoulis et al. 2002; Fang et al. 2006; Hashimoto et al. 2010). However, the high-resolution $H\alpha$ observations with the Swedish 1 m Solar Telescope (SST; Scharmer et al. 2003) present morphological evidence for the photospheric origin of EBs (Watanabe et al. 2011).

In order to understand the physical mechanisms behind EBs, several authors performed nonlocal thermodynamical equilibrium (NLTE) calculations from best-fit ad hoc perturbations of a static one-dimensional (1D) solar atmospheric model (Kitai 1983; Fang et al. 2006; Socas-Navarro et al. 2006; Berlicki et al. 2010; Bello González et al. 2013; Berlicki & Heinzel 2014; Grubecka et al. 2016). Kitai (1983) modeled the $H\alpha$ line by adding a constant temperature and density enhancement within a specific height range above the quiet-Sun atmosphere of Vernazza et al. (1981) and then performed

an NLTE calculation to derive a temperature excess of 1500 K and a five times denser atmosphere in the height range of 700–1200 km. Fang et al. (2006) included the Ca II 8542 Å line in addition to the $H\alpha$ line obtained with THEMIS telescope (Mein & Rayrole 1985) to derive a temperature enhancement of 600-1300 K in the thermal models, and 100-300 K if the nonthermal effects are included. Bello González et al. (2013) after performing a more sophisticated 2D modeling, found that the heating, as well as an increase in the H α opacity, is likely to occur at heights of 300-800 km. Moreover, they were able to reproduce line shifts and profile asymmetries induced by lineof-sight velocities at those heights and also at higher atmospheric layers. They found that the EBs occurred at regions where the longitudinal magnetic field shows opposite polarities, which indeed suggests that magnetic reconnection is likely the cause of the H α brightening. Berlicki & Heinzel (2014) compared their synthetic H α line profiles with observations performed with the Dutch Open Telescope (DOT; Rutten et al. 1997) finding a temperature excess of 5000 K over the extent of 400 km at the height of 1000 km. Yang et al. (2016) estimated ΔT in the range of 400–2000 K in the EB using the indirect measurement with a large scatter in the predicted temperature excesses depending on the models

Contrary to the static model-based approaches, EBs often exhibit highly dynamic features such as upward motions of recursive small-scale heating events comprising of very bright, rapidly flickering, flame-like features that appear intermittently (Watanabe et al. 2011) and the bimodal-jet pattern and upward extension (Vissers et al. 2015). The dynamic nature suggests that nonequilibrium hydrogen ionization/recombination among the lines examined on Rutten (2016) may invalidate the traditional 1D static perturbation assumption. Accordingly, more realistic time-dependent 3D magnetohydrodynamics

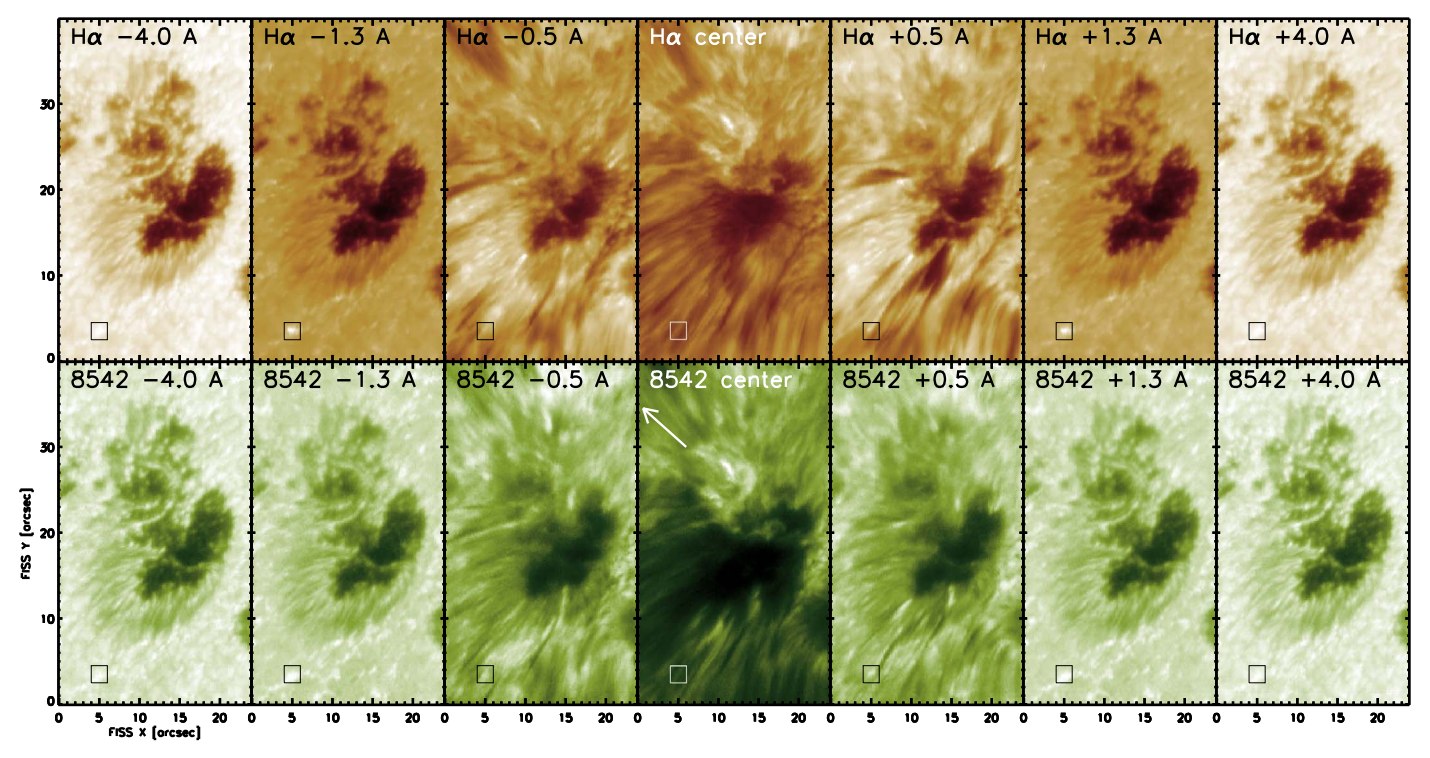


Figure 1. FISS raster images of NOAA AR 12080 at 17:38:18 UT on 2014 June 5. The target EB is marked with the rectangular box in the lower left corner of each panel. Seven wavelengths are selected for this display for the H α line (top panels) and the Ca II 8542 Å line (bottom). Each image is centered at (-510'', -200''). The arrow in the lower-middle panel indicates the limb-ward direction. Note that each image is scaled individually, and the EB brightness within the box does not necessarily correspond to the profiles in Figures 3 and 4.

(MHD) simulations have been performed by Hansteen et al. (2017) and Danilovic (2017) where the characteristic $H\alpha$ wing enhancement of EBs is produced through magnetic reconnection at photospheric levels.

In this paper we analyze high-resolution EB spectra at the $\rm H\alpha$ and Ca II 8542 Å lines obtained with the Fast Imaging Solar Spectrograph (FISS; Chae et al. 2013) installed on the 1.6 m Goode Solar Telescope (GST; Goode et al. 2010) in the Big Bear Solar Observatory (BBSO). We perform an NLTE simulation of the static 1D plane-parallel model atmosphere, and, thus, we cannot address any dynamic features of EBs. However, our investigation includes the time series of spectral lines, by which we may determine the temporal variation of the EBs atmosphere. We complement the two-line study by additional NLTE calculations of the Na I D₁ and Mg I b₂ lines subject to the published properties of EBs, as well as that of UV continuum at 1600/1700 Å observed by the Atmospheric Imaging Assembly (AIA; Lemen et al. 2012) on board the Solar Dynamics Observatory (SDO). Those lines have different heights of formation and sensitivity to EBs, thus, examining them together will allow us to set additional constraints for inferring the properties of that interesting phenomena.

2. Data

The data examined in this work were obtained using two bandwidths of FISS: $6562.8 \pm 5 \, \text{Å}$ for the $H\alpha$ and $8542.3 \pm 6.5 \, \text{Å}$ for the Ca II $8542 \, \text{Å}$ lines. The spatial resolution of these images is $\sim\!0.''3$. FISS does not reach the highest resolution $\leq\!0.''1$ available to other Fabry–Pérot interferometer-based instruments installed on the $1.6 \, \text{m}$ GST, because it obtains images and spectra by scan of the slit across the field of view at cadence $\sim\!16 \, \text{s}$, and the post-imaging processing, speckle reconstruction, is usually

unavailable. The spatial resolution of FISS is, however, good enough to ensure that the EB intensity profiles are free of the effect of the surrounding quiet-region profiles. The main advantage of FISS is its high spectral resolving power $\sim\!140,\!000$ as achieved by using an echelle grating as the main spectral element with the aid of interference filters for the order sorting. This gives the net spectral resolution of 45 mÅ for the H α line and 64 mÅ for the Ca II 8542 Å line when slits of width 32 μ Å are used (Chae et al. 2013, their Table 5).

Figure 1 shows the multiwavelength raster images of the target EB (marked with a rectangular box in each panel) and the associated active region, NOAA AR 12080 at 17:38:18 UT on 2014 June 5. From left to right, the wavelength increases from -4 Å with respect to the line center of the H α (top) and the Ca II 8542 Å (bottom) spectral lines. Images at seven selected wavelengths are shown as denoted in each panel. The center of each image is at (-510'', -200'') and the cosine of the heliocentric angle is 0.81. The EB started at 17:24:26 UT and ended at 17:43:32 UT, during which we obtained 52 snapshots. We note that the EB is most conspicuous at ± 1.3 Å from the center of each line, and tends to disappear at wavelengths closer to the line center. It is thus likely that the EB is located underneath the fibril canopy, which is strong enough near the center of the lines to occult the EB. This alone suggests that the EB must be either a photospheric or a low chromospheric phenomenon (see Rutten et al. 2013, their Figure 3). FISS has detected additional EBs events, but most of them exhibit significant line asymmetry. This implies mass motions (Fang et al. 2006), which requires dealing with line-of-sight velocity perturbations on top of the temperature enhancements to explain the intensity brightening. The present event was selected because the EB spectrum shows an almost symmetric

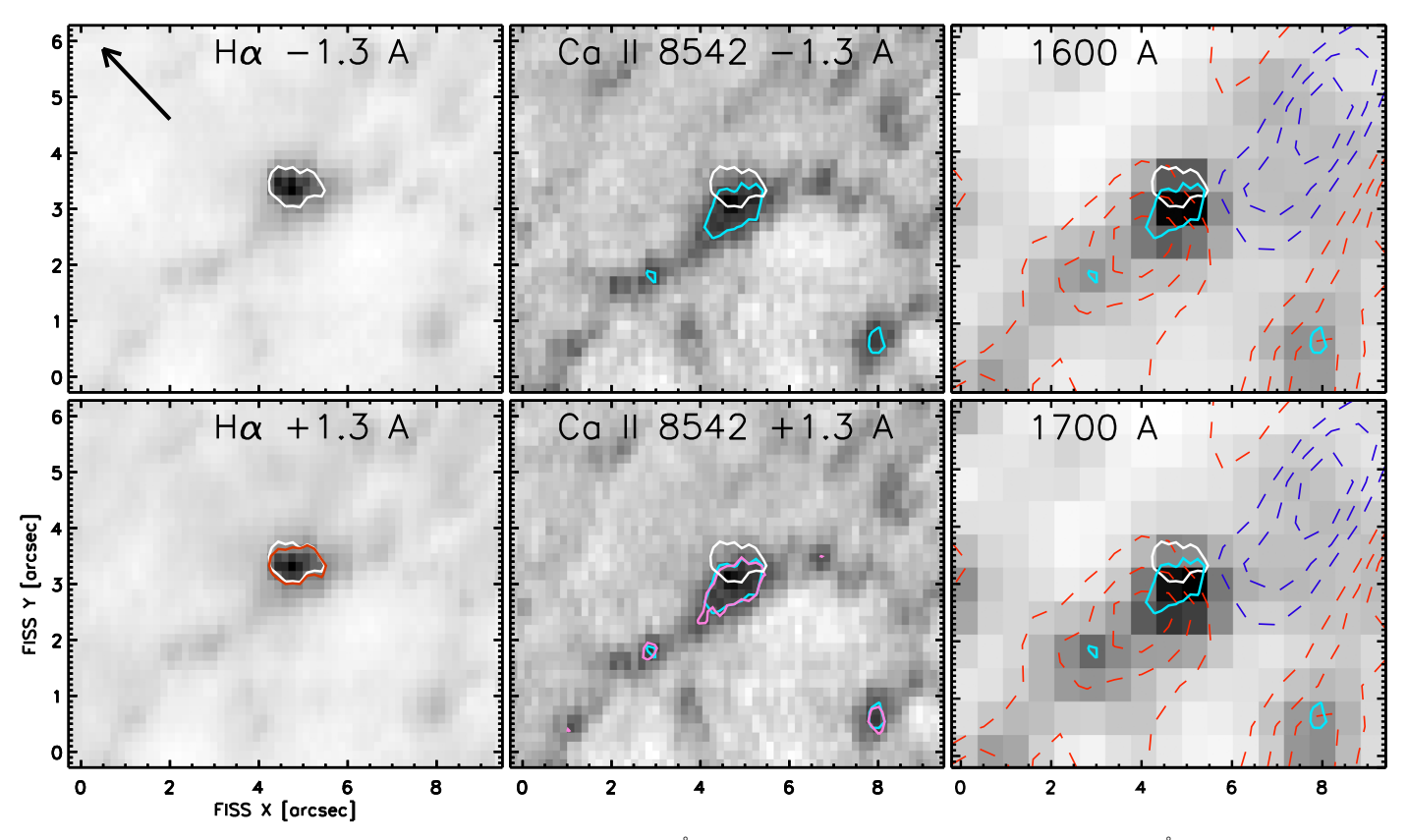


Figure 2. Morphologies of the EB at FISS H α wings (first column), Ca II 8542 Å wings (middle column), and the SDO/AIA 1600/1700 Å (last column). The region is around the inset box of Figure 1 at 17:38:18 UT and the limb direction is indicated by the arrow in the top left panel. The intensities in all wavelengths are plotted in the inverted grayscale. The detection contours based on the H α blue wing (white) and Ca II 8542 Å blue wing (azure) enhancements are also plotted in other panels for comparison. The detection contours for the corresponding red wings are displayed in red and purple. The last column includes the HMI line-of-sight magnetogram in the dashed contours in the levels of ± 40 , ± 80 , and ± 120 G. Red (blue) contours represent the positive (negative) magnetic polarity.

intensity profile. This allows us to focus only on the temperature diagnostics.

Figure 2 shows close-up views of the EB in the region around the inset box defined in Figure 1. The intensity is displayed using an inverted grayscale color code, i.e., black indicates higher intensity. The first column depicts the $H\alpha$ blue wing (top) and the red wing (bottom) intensity signal. The highlighted area enclosed by the white contour represents enhanced pixels on the $H\alpha$ blue wing (50% of the maximum EB intensity). This contour is included in the rest of the panels for comparison purposes. Also, we added an arrow to indicate the limb-ward direction.

Starting with the red wing intensity panel (left bottom), we can see that there is not much difference between the morphologies at the blue (white) and red wings (red contour) with both events showing a slight limb-ward extension. Likewise, the middle column shows the Ca II 8542 Å blue wing detection contour (azure) and the red wing (purple), which also nearly coincide with each other. However, the intensity of the Ca II 8542 Å wing is rather extended perpendicular to the limb-ward direction, unlike that of the H α wing.

In the rightmost column, AIA 1600 Å (top) and 1700 Å (bottom) continuum bands are displayed along with the line-of-sight magnetic field data (dashed contours) from the Helioseismic and Magnetic Imager (HMI; Schou et al. 2012) on board the SDO. The two continuum regions are very similar to each other, with their maximum intensity coincident with the areas where the wings of H α and Ca II 8542 Å are enhanced

(see the contours). Their morphologies seem closer to that in the Ca II 8542 Å wing rather than in the H α wing in this event. Whether or not this is a common property of EBs needs to be checked with more samples. The HMI longitudinal magnetic field distribution shows that the EB is located near the magnetic polarity inversion line, supporting the idea that EBs are the result of a magnetic reconnection process.

Both the limb-ward extension of the $H\alpha$ wing intensity and the perpendicular extension of the Ca II 8542 Å wing intensity are in agreement with previous works (Vissers et al. 2013, their Figure 3). The first property is consistent with the tall and slender structure of the $H\alpha$ EB observed by Watanabe et al. (2011), and the second property is yet to be explained. We note that, in the present case, the orientation of the Ca II 8542 Å wing intensity is also in the direction away from the spot center, thus parallel with the penumbral structure. On the other hand, Vissers et al. (2013) found the opposite, namely, the structure extended across the penumbral structure. It is thus inconclusive which one is a more critical factor with these two samples only.

Another remarkable property is that the common morphological pattern of the Ca II 8542 Å wings and that of the AIA 1600/1700 Å continuum is, in fact, present in the H\$\alpha\$ wing images too. It is that the H\$\alpha\$ EB is much brighter than other bright regions to stand out in a distinct morphology. The other bright locations, given the HMI magnetogram, seem to be associated with magnetic field concentrations in the networks. The most apparent morphological difference is the small but finite offset between the H\$\alpha\$ wing maximum point and that of

the Ca II 8542 Å. It might be that the $H\alpha$ source better represents hot particles ejected in the upward direction to be extended limb-ward, whereas the Ca II 8542 Å source, are thermalized particles in the low photosphere. In that case, the morphological difference may be accompanied by the Doppler motion, for which we, however, see no signature in this event selected under the criterion of the line symmetry.

3. Methodology

We make use of the RH code (Uitenbroek 2001) to synthesize the intensity profile of different lines of interest. We focus on H α , Ca II 8542 Å, Na I D₁, and Mg I b₂ lines, and the continuum bands at 1600 and 1700 Å. Starting with the first transition, we use a 6 level atom included in the code's default library. The atom contains, among others, the Ly α and β as well as the Balmer α and β lines. We switch on partial redistribution (PRD) effects for the former lines while the latter are treated under complete redistribution (CRD). In the case of the Ca II 8542 Å we employ a 6 level atom (see, for instance, Shine & Linsky 1974) and we treat all the lines under CRD. The lower chromospheric Fraunhofer lines are also treated assuming CRD with the Na I D lines computed using a 12 level atom presented in Bruls et al. (1992), while the Mg I b lines are generated with the simplified 6 level atom of Quintero Noda et al. (2018). In the case of the continuum bands at UV wavelengths, i.e., 1600 and 1700 Å, we include all the spectral lines described in the Kurucz database (Kurucz & Bell 1995) for that spectral region. We treat those UV transitions assuming local thermodynamic equilibrium (LTE) while all the previously mentioned lines, i.e., $H\alpha$, Ca II 8542 Å, Na I D_1 , and Mg I b₂, are computed under the NLTE assumption. Moreover, in every case, we also compute the continuum background opacities taking into account different metal species, a total of 11 including H, Fe, C, O, N, Mg, Na, Ca, S, Si, and Al. In the case of Fe, O, N, S, Si, and Al, the main transitions for the neutral and single ionized states are considered while, for the rest of the elements, only the transitions of the neutral state are considered. We also take into account the effect of molecules on the background opacities considering 12 of the most common ones. Finally, although we compute the atomic populations of the mentioned transitions every time we use a different atmospheric model, we do not consider the impact that the changes on those populations have on the total electron density of the atmospheric models (for more information, see the works of Bello González et al. 2013; Berlicki & Heinzel 2014). The reason is that, after a test using RH, we realized that the inserted temperature perturbations, if extended only over a very narrow range of heights, do not change the electron density significantly enough to produce a noticeable impact on the final synthetic profiles.

4. H α and Ca II 8542 Å Lines

We adopt the classical procedure of the EB atmosphere modeling (Berlicki & Heinzel 2014; Grubecka et al. 2016) in which one or a few temperature humps (ΔT) specified by choice of height (h) and width (Δh) are added to a quiet-Sun model atmospheric temperature, T(h). With such a 1D model atmosphere, we perform an NLTE calculation using the aforedescribed method to produce synthetic line profiles for comparison with the observed FISS profiles. For the quiet-Sun atmosphere, we use the semi-empirical FALC model

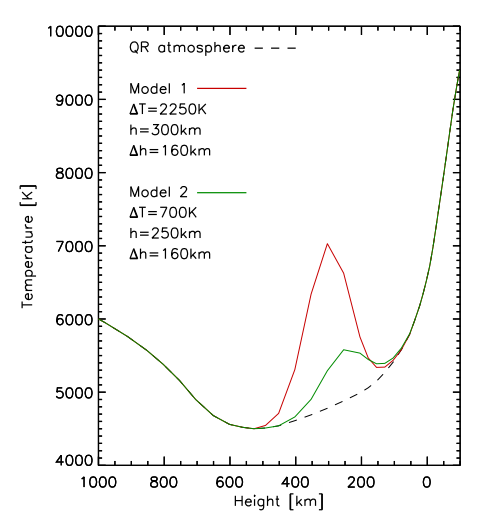
(Fontenla et al. 1993), as it reproduces the atlas relatively well. In addition, although this type of study has been done before, the main advantage of the present work is that the instrument FISS provides high spectral resolution observations over a broad spectral range, which will impose additional constraints on the atmosphere modeling.

Before the spectral analysis, we check a couple of spatial properties learnt from Figures 1 and 2. First, the EB emission at wavelengths near each line center is likely to be influenced by the fibril lying above it. We therefore calculate the whole profiles but exclude, from the test of the goodness of our models, the line cores, specifically, $|\Delta \lambda| < 0.5$ Å from the H α line center and $|\Delta\lambda| < 0.25 \,\text{Å}$ from the Ca II 8542 Å line center to focus on reproducing the line wings. Second, the morphological differences between the H α and the Ca II 8542 Å line sources suggest that use of the 1D plane-parallel atmosphere might be inadequate. We nevertheless proceed with this 1D static model atmosphere mainly because its relatively simple and fast to perform the computations with the RH code, and compare the calculated synthetic line profiles with FISS observed spectra. However, we delve further into the possible shortcomings of this approach in Section 5.

We present the results in Figures 3 and 4 with the temperature stratification in the left and the intensity profiles of H α (upper) and Ca II 8542 Å (lower) in the rightmost panels. In each figure, the quiet-Sun model temperature is plotted with a dotted line and a reference quiet-Sun profile, computed as the averaged intensity over a quiet-Sun region, with a dashed line. The FALC model reproduces that reference profie very well; though, we opted not to show it in the figures for simplicity. The goodness of the fit, χ^2 , defined as $\sum_k (I_k^{\rm FISS} - I_k^{\rm RH})^2/I_k^{\rm RH}$ is computed for each model and included inside each panel. Here $I_k^{\rm FISS}$ is the intensity observed by FISS at kth wavelength and $I_k^{\rm RH}$ is the synthetic intensity computed using the RH code at that wavelength. Index k runs within each line profile except for the line core wavelengths mentioned above.

4.1. Broad Hump Model

We set the height, h, of the EB formation in the range of $50 \,\mathrm{km} < h < 850 \,\mathrm{km}$ at height intervals of $50 \,\mathrm{km}$, i.e., a total of 17 grid points in height. The EB atmosphere is modeled by adding a single Gaussian temperature hump over the quiet-Sun FALC atmosphere. The FISS spectra and synthetic products shown in Figure 3 pertain to the time of maximum EB brightness at 17:38:18 UT. When each model is allowed to have a different set of parameters, regarding height, location, and temperature amplitude, model 1 corresponds to the best fitted atmosphere for the ${\rm H}\alpha$ line while model 2 is the one that produces the best result for the Ca II 8542 Å line. On the one hand, we found that, in order to fit the H α line, we need to insert a temperature enhancement as high as \sim 2600 K. On the other hand, to match the Ca II 8542 Å line, only a lower temperature enhancement $\sim 1000\,\mathrm{K}$ is needed. The width and location of the temperature hump are not the same but similar to each other: $h = 300 \, \mathrm{km}$ for the H α line and 250 km for the Ca II 8542 Å line. Hence, there is no particular impediment on reproducing the observed intensity profiles using two independent (and different) atmospheric models. However, it is clear that none of those models is able to fit both lines simultaneously. We need a high temperature enhancement for reproducing $H\alpha$, which results in excessive heating for the Ca II 8542 Å line. Conversely, a modest temperature enhancement accurately reproduces the Ca II 8542 Å profile, but only produces a weak H α wing enhancement.



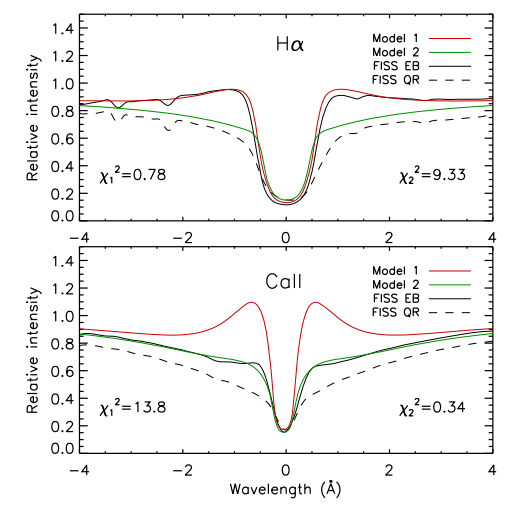


Figure 3. Single hump models for the EB lines observed at 17:38:18 UT. Left: the temperature structures of the best-fit single hump model 1 (red line) that best fits the FISS H α line and model 2 (green) that best fits the Ca II 8542 Å line, along with the quiet-region model (dotted). Right: the synthetic line profiles of models 1 and 2 are plotted together with the observed lines with the FISS profiles from the EB (black) and the quiet region (dashed) for the H α (top panel) and the Ca II 8542 Å line (bottom).

Based on these results, we believe that a single hump model is unable to reproduce both spectral lines as far as the EB heating occurs over a relatively broad height range ($\Delta h > 100 \, \mathrm{km}$).

In addition, we have also calculated the profiles from double hump models (not shown) to check if the two lines are sensitive to different atmospheric layers. It turns out that the double hump model shows little improvement over the single hump model unless the two humps are well separated in height, say, farther than the width Δh . It instead appears that the heights of the temperature hump for the two lines need not be very different from each other, and the difficulty in simultaneously reproducing both lines may not be attributed to the different formation heights of the two lines.

4.2. Narrow Hump Model

Gathering the results from the previous studies, we have that the temperature enhancement should be high enough to fit the observed H α wing intensity. Unfortunately, when computing the Ca II 8542 Å line profile using that high temperature enhancement the resulting spectrum does not match that observed by FISS. Based on the study of the Ca II response functions presented in Quintero Noda et al. (2016), we reached the conclusion that the temperature enhancement, ΔT , should be confined to a narrow height range, say $\Delta h \lesssim 100 \,\mathrm{km}$. Moreover, we can include that perturbation at a location to which the Ca II 8542 Å line is not very sensitive so that it does not bring up the Ca II 8542 Å line intensity too much. This will work for $H\alpha$ as well, because of the wings of the spectral line, where the EBs leaves their imprint, seems to respond to a temperature enhancement in a different range of geometrical heights. Specifically, this range of heights corresponds to the lower photosphere, probably below $\log \tau = -2$, based on the response functions to temperature presented in Socas-Navarro & Uitenbroek (2004). Therefore, the height where the wings of the intensity profile are most sensitive to temperature variations seems to be located more profoundly in the atmosphere in the case of $H\alpha$.

We thus try a single temperature hump with a very narrow width. To adequately represent such a thin temperature

structure, we had to use a finer grid for the model atmosphere than that of the original FALC model. The available FALC model included in the RH library has a height step of 50 km in the region of interest (below $h = 500 \,\mathrm{km}$). For this reason, we interpolated that range of heights to a finer grid of 5 km height steps, while the heights outside that range remained unchanged. The number of grid points increased from 82 to 165, and the computing time accordingly. Model a that we built with a single temperature hump with a thickness of $\Delta h = 20 \,\mathrm{km}$ is shown in the top panel of Figure 4. The best-fit height $h = 120 \,\mathrm{km}$ is somewhat lower than that of the above models, h > 300 km. However, Model a can fit both lines relatively well, with the most significant differences for the case of the Ca II 8542 Å line. It, therefore, seems that the EB of interest is produced by a localized heating event (around 20 km width) that takes place at photospheric heights. Based on these encouraging results, we examined different time intervals of the evolution of the EB event, at 17:37:11 UT and 17:27:26 UT. These models, denoted as b and c, are shown in the next two panels of Figure 4. The best fitting requires the same thickness, and only the temperature enhancement and the height need to be adjusted. According to the results obtained with the narrow hump models, the heating at the early stage of the EB is weak and occurs even at a more profound layer ($h = 60 \,\mathrm{km}$) in the photosphere and moves to higher heights ($h = 120 \,\mathrm{km}$) as the EBs' intensity increases.

4.3. Temporal Evolution

We repeat the spectral analysis using the narrow hump model for all time intervals during the EB activity, which consists of 52 frames from 17:24:26 to 17:43:32 UT. Figure 5 shows, in the left panel, the summary plot of the derived best-fit height h and the amount of temperature excess ΔT as functions of time. The right panel shows the EB wing intensities of both lines for comparison. For this study, based on the previous results, we kept fixed the width of the Gaussian perturbation to 20 km, simplifying the fitting. At the early and quiet phase, the EB occurs at a lower height down to h = 50 km and then moves to higher layers reaching up to 120 km at the time of

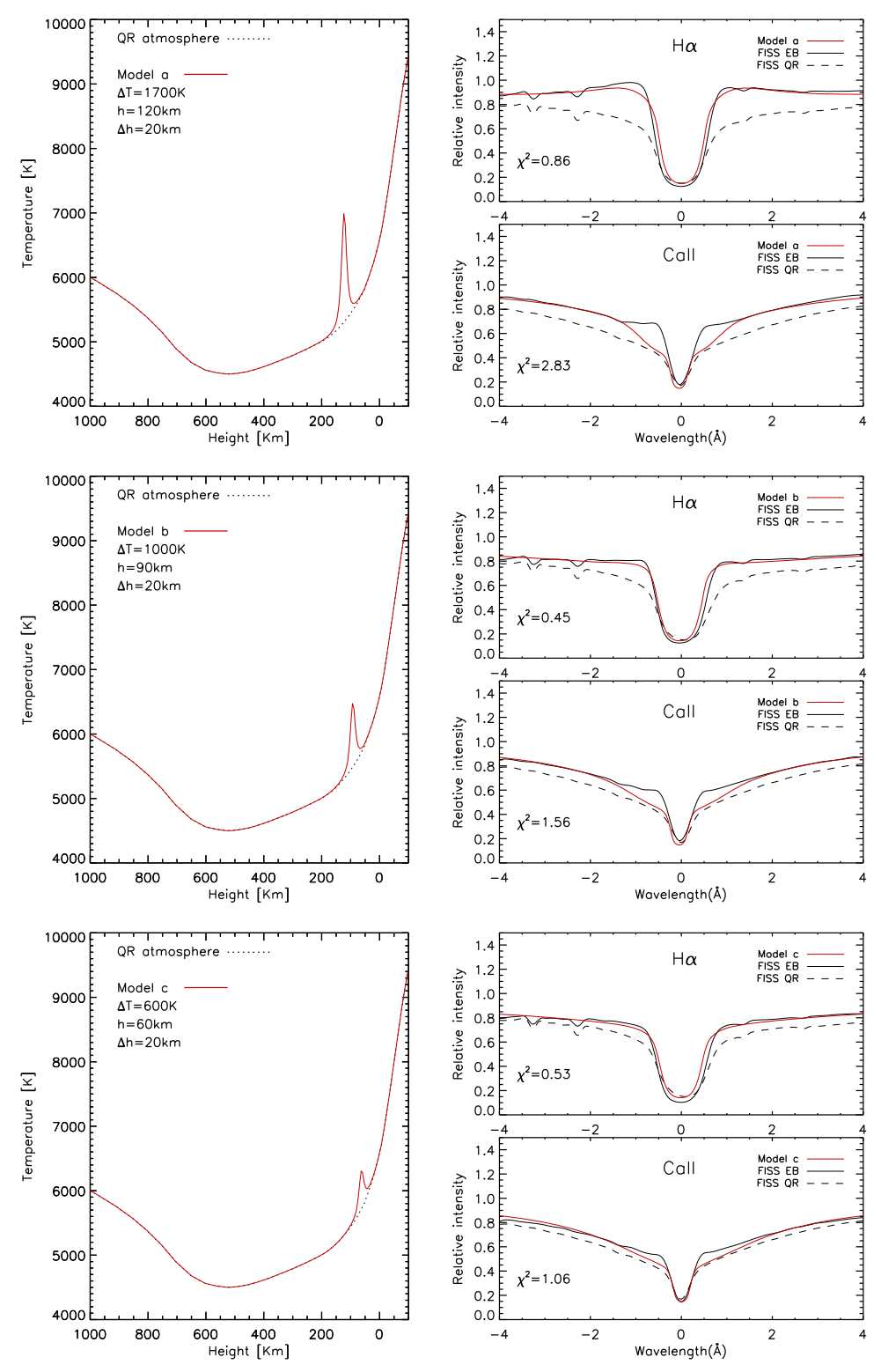


Figure 4. Narrow hump models ($\Delta h = 20$ km) for the EB lines at three different times: 17:38:18 UT, 17:37:11 UT, and 17:27:26 UT from top to bottom. Otherwise, the same plot convention as in Figure 3 is used.

maximum intensity. During the lifespan of this event, the $H\alpha$ and the Ca II 8542 Å lines show a rapid increase and decrease in intensity (see Bello González et al. 2013; Yang et al. 2013; Vissers et al. 2015). The electron temperature derived from the best-fit models also follows the trend shown by the $H\alpha$ and the Ca II 8542 Å wing intensity. The rise timescale is $\sim\!\!1$ minutes, much shorter than the lifespan of the EB lasting $\sim\!\!10$ minutes

while the decay is also similarly short, which implies that the cooling is very efficient. Such a high cooling rate is likely to happen in the photosphere, full of dense and cool particles. It follows that one EB event must consist of multiple heating events. If each heating event should be attributed to magnetic reconnection, then the EB involves various small-scale reconnection events. The result shown in Figure 5 suggests

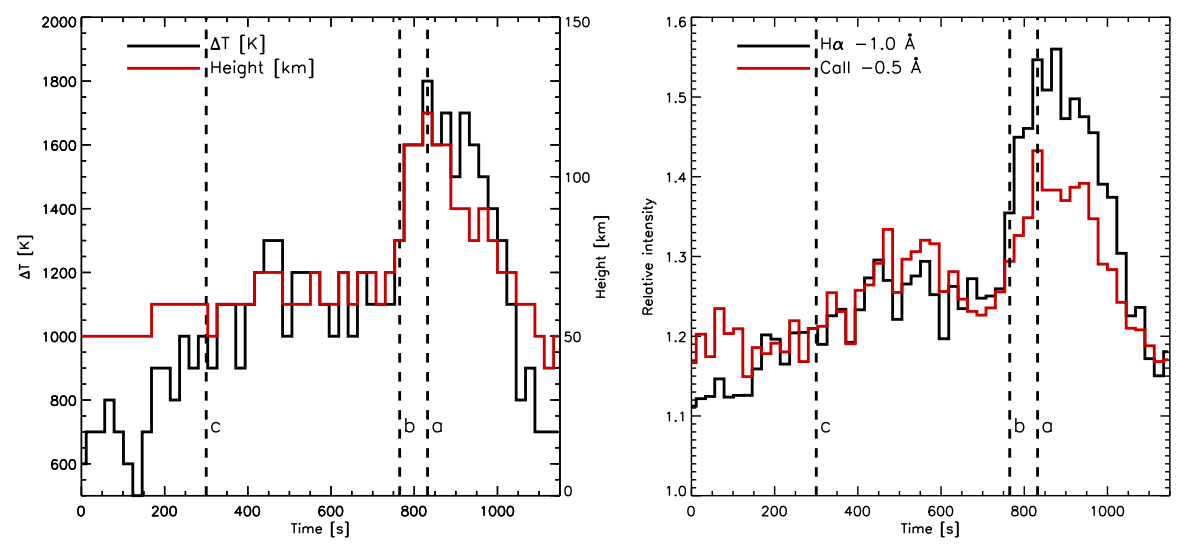


Figure 5. Temporal evolution of the EB wing intensities and the best-fit model parameters. Left panel: temperature enhancement ΔT (black) and height h (red) of the best-fit model. Right panel: intensities at the H α –1.0 Å (black) and the Ca II 8542 Å –0.5 Å (red). Time is given in units of second starting from 17:24:26 UT. The three vertical dashed lines denoted a, b, and c indicate the times of the spectral profiles plotted in Figure 4.

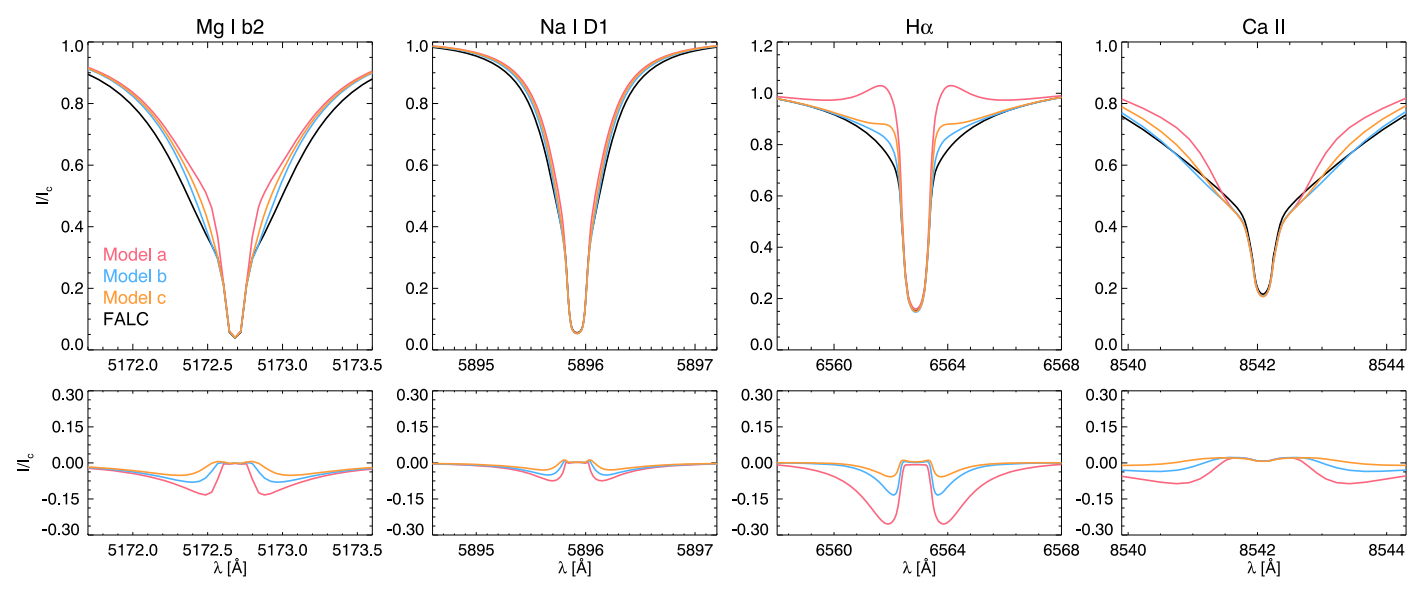


Figure 6. Synthetic spectral lines of Mg I b_2 and Na I D_1 along with H α and Ca II 8542 Å. The top row displays the profiles calculated with the three EB atmospheres (colored lines) and the original FALC model (black lines). Bottom panels depict the difference for each case with respect to the reference result from the FALC atmosphere.

that each event of the magnetic reconnection could occur at a different height and the height can rapidly change, for instance, from h = 70 to 120 km in 44 s. A timescale that is, again, much shorter than the whole lifespan of the EB.

5. Additional Spectral Lines and the UV Continuum

5.1. Na I D_1 and $Mg I b_2$ Transitions

Previous works, for instance, Rutten et al. (2015), pointed out that EBs are mainly visible in the wings of the $H\alpha$ line while there is no trace, or just a weak impact, on the intensity spectrum from different upper photospheric/low chromospheric lines like Na I D_1 and Mg I b_2 transitions. In this regard, we would like to further support our conclusion about the nature of EB as a narrow temperature perturbation at lower atmospheric layers. For this purpose, we synthesize the Mg I b_2 and the Na I D_1 spectral lines using the three atmospheric

models shown in Figure 6 by the method explained in Section 3. The resulting profiles are displayed in the top row of Figure 6 while the bottom row represents the differences with respect to the results from the original FALC model, the reference atmosphere where we inserted the temperature hump.

Starting with the neutral magnesium transition, we can see that the temperature hump (see colors) changes the width of the line, enhancing its wings at the same time. The same happens with the Na I D_1 line, although with much less relative impact. In the case of the $H\alpha$ line, we can see that the hump largely enhances the wings in comparison with the results of the quiet-Sun FALC atmosphere, something that was required to fit the observed FISS spectra. Finally, in the case of the Ca II 8542 Å transition (rightmost panel), the effect again takes place in the far wings, also allowing us to match the observed spectra at those wavelengths (see Figure 4). This means that the hump at lower layers has an impact mainly on the wings of traditional

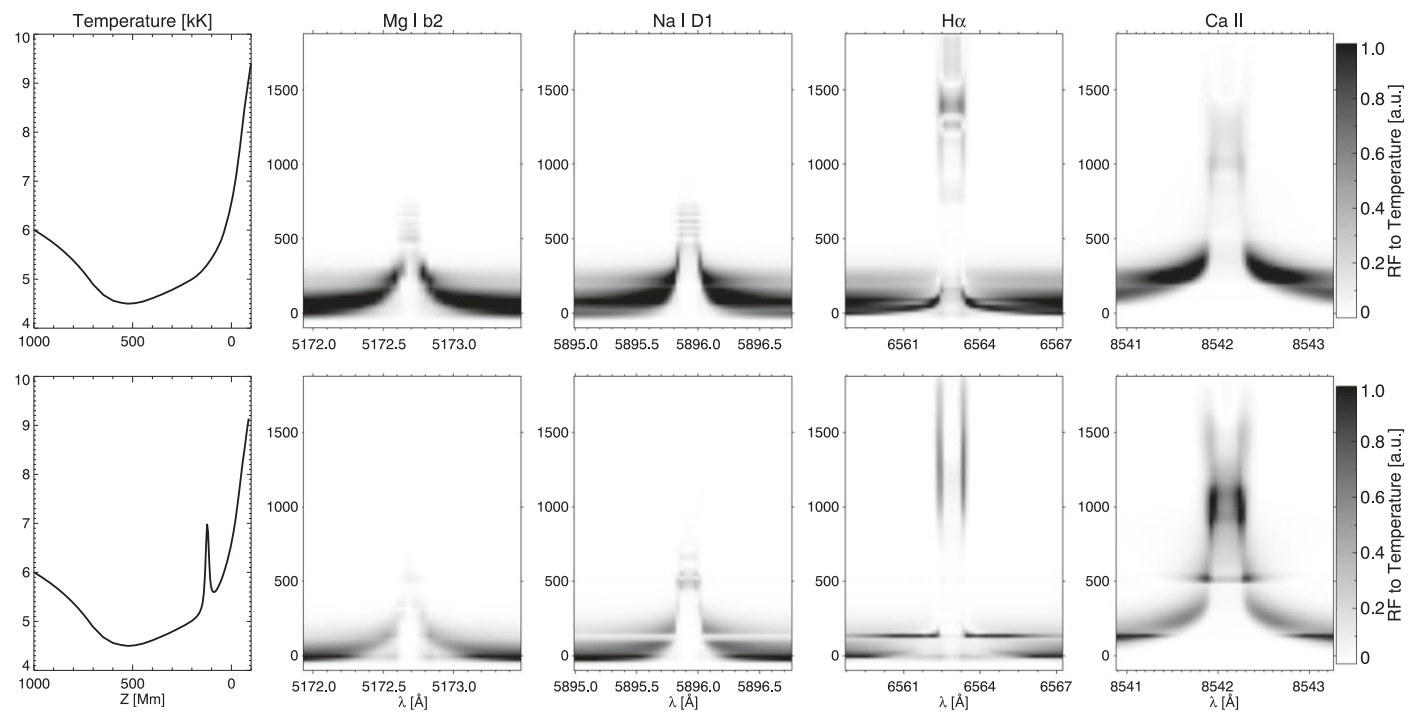


Figure 7. Response functions to temperature perturbations for the four lines using the FALC (top) and Model *a* atmospheres (bottom). We represent in the leftmost column the corresponding temperature stratification of each model. Regarding the RF panels, we used an inverted grayscale color code, i.e., dark means sensitivity to temperature perturbations while white indicates no response.

chromospheric lines except in the case of $H\alpha$, that shows a strong enhancement mostly at the inner "wings" of the line, similar to the expected behavior of EB events. Thus, our proposed and simplistic scenario is not only able to reproduce the observed $H\alpha$ and Ca II 8542 Å spectra, but also preserves the properties of the EB for different spectral lines because, as explained in Rutten et al. (2015), EB events do not enhance (at least not strongly) the $Na I D_1$ and $Mg I b_2$ lines.

5.2. Response Functions to Temperature Perturbations

We continue delving into the properties, and their effect on the different spectral lines, of the created atmosphere with a temperature hump versus those of the original FALC atmospheric model. In this regard, we compute the response functions (Landi Degl'Innocenti & Landi Degl'Innocenti 1977) to temperature changes for the same lines studied in the previous section. We follow the method explained in Quintero Noda et al. (2016) introducing a small, in comparison with the atmospheric values, temperature perturbation of ± 1 K amplitude, at different heights and we examine how the spectral lines respond to it. To improve the visualization of the response functions, we only focus on two atmospheric models: the original FALC and Model a (the one with the strongest temperature hump) of Figure 4. The results, as well as the temperature stratification for each case, are presented in Figure 7.

Starting with the FALC atmosphere (top) we can see that the Mg I b₂ and Na I D₁ lines are sensitive to temperature changes at lower heights, through their wings, and upper photospheric layers at line core wavelengths. The reason why the lines are only sensitive at lower layers to temperature, while their sensitivity to the rest of atmospheric parameters lies at much higher layers, e.g., Eibe et al. (2001) and Quintero Noda et al. (2018), was explained in Rutten et al. (2011). Concerning the

 ${\rm H}\alpha$ and Ca II 8542 Å lines, the behavior is entirely different showing that the core wavelengths reach very high in the atmosphere. Interestingly, we can see that ${\rm H}\alpha$ does not show a smooth transition from the heights covered by its wings and line core wavelengths. The wings are primarily sensitive only to lower heights, while the line core wavelengths jump directly to the chromosphere.

Now moving into the RF to temperature changes for the second atmospheric model (bottom), we can see that the RF for Mg I b₂ and Na I D₁ are the same as those shown in the top row. There is some effect on the latter in the form of a horizontal band at similar heights to those of the hump. However, the RF intensity in this region is, in fact, lower (white means less sensitivity), what can happen if we had increased the ionization degree with the temperature hump. Regarding $H\alpha$, there is a significant enhancement of the RF at similar heights to that of the temperature hump, indicating that, indeed, the spectral line is susceptible to that perturbation. Moreover, the enhancement only takes place at a narrow wavelength region corresponding to the inner wings of the spectral line, where the EB signature are traditionally found. This explains why Model a was able to match the observed FISS spectra. Finally, the Ca II 8542 Å response function shows also an enhancement at lower layers, and at the far spectral wings at the same height where the temperature hump was inserted. We believe this is the reason behind the increase of the outer wing intensity found in Figures 4 and 5.

5.3. Synthetic Profiles of the UV Continuum at 1600 and 1700 $\mathring{\rm A}$

We mentioned in the Introduction and also in the description of Figure 2 that there are traces, concerning intensity enhancements, on the UV bands at 1600 and 1700 Å cospatial

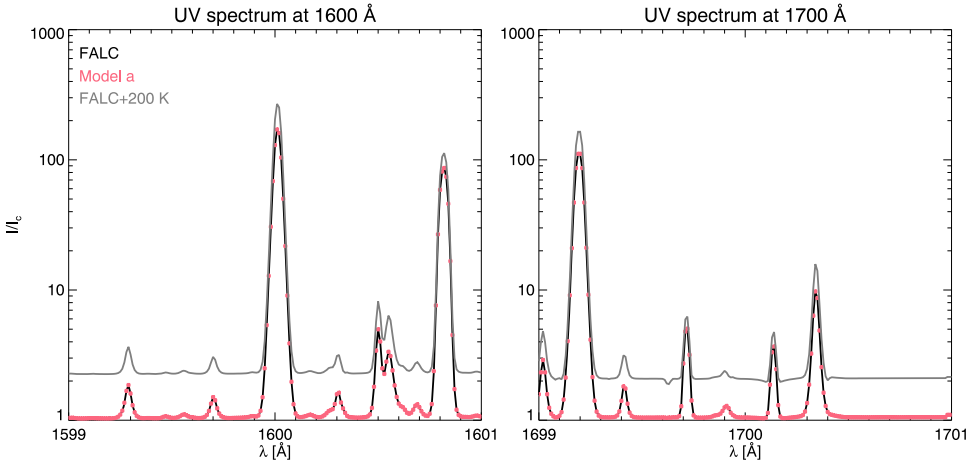


Figure 8. Synthetic UV spectra at 1600 Å (top) and 1700 Å (bottom). Black designates the original FALC atmosphere while red squares depict the results from the Model *a* presented in Figure 4. We included an additional temperature perturbation to the FALC model, adding 200 K at all heights, that produces the gray-colored profile. Each spectrum is normalized to its local continuum intensity.

with the pixels that show EB features in $H\alpha$. Therefore, to continue to deepen on the capabilities of a narrow temperature hump to explain the observational properties of EB, we synthesize the two UV spectral regions using the two atmospheres presented in Figure 4, i.e., Model a and the original FALC model. The results are shown in Figure 8 where solid black corresponds to the unperturbed FALC model, and red squares designate the synthetic spectra from Model a. In this occasion, they appear to be identical, which indicates that the temperature enhancement introduced at lower layers does not reach the UV continua. We thus perform an additional simple test in which we add 200 K over the full range of heights covered by the FALC atmosphere (gray-colored lines). In this case, the continuum is indeed enhanced indicating that, although we do not need a large temperature hump to modify the UV spectra, we have to increase the temperature at different layers, higher in the atmosphere, to properly account for the UV brightenings found in the EB observations.

6. Discussion

We presented a multiwavelength analysis of an EB by performing the NLTE computation of the H α and the Ca II 8542 Å synthetic profiles constrained by high spectral resolution (\lesssim 45 mÅ and \lesssim 64 mÅ, respectively) observations performed with the FISS instrument. This was complemented with additional calculations of the Na I D₁ and Mg I b₂ lines and the UV continuum at 1600 and 1700 Å for comparison with the SDO/AIA observation. Such multiwavelength diagnostics for the EB properties have not yet been addressed elsewhere.

The first difficulty that we have encountered is that, with a modest thickness of the temperature hump ($\gtrsim\!100\,\mathrm{km})$ in the low chromosphere, both the H\$\alpha\$ and the Ca II 8542 Å line profiles cannot be simultaneously reproduced. We propose a rather unusual EB atmosphere with the temperature hump placed at a thin photospheric layer ($\lesssim\!20\,\mathrm{km}$) to replicate the wing enhancement of both lines, because the atmosphere keeps the response of the Ca II 8542 Å line low and that of the H\$\alpha\$ wing response sufficiently high. Besides, we have shown that the thin temperature hump located in the photosphere does not have a significant impact on the Mg I b2 and Na I D1 lines, which is consistent with previously published results (Rutten et al. 2015, their Figure 5). In comparison, the H\$\alpha\$ line detects

the temperature hump at the inner wings, but not at core wavelengths, similar to the traditional EBs spectral signature. The Ca II 8542 Å line, however, is sensitive to that perturbation mainly in the wings, which allows us to match the observations accurately. Hence, if we want to simultaneously reproduce the enhanced H α line wing and a relatively normal Ca II 8542 Å profile, we should increase the temperature in a narrow range of photospheric layers. This result together with the undetectability of EB on the Na I D₁ and Mg I b₂ lines suggests that the temperature hump must be in the photosphere. We were, however, unable to reproduce the intensity enhancement on the UV 1600 and 1700 Å spectral regions, something found in AIA observations of EB events. We believe that the reason is a lack of "global" temperature enhancement that would extend to upper layers and that it is not necessarily as large as the temperature hump introduced at lower heights, but should be high enough to enhance the UV continua. Moreover, this moderate temperature increase may also improve the Ca II 8542 Å line core fits presented in Figure 4. Therefore, we plan to strengthen our simplistic model in the future starting from this hypothesis.

By applying the 1D static model atmosphere to the FISS data in additional observing times, we found that the height where we need to insert the temperature hump evolves moving to upper layers from ${\sim}40~\text{km}$ to ${\sim}120~\text{km}$. We also found that the timescale of the EB's height and intensity variations is ${\lesssim}1~\text{minutes}$, much shorter than the ${\sim}19~\text{minutes}$ of the EB's lifetime, which allows us to conclude that the EB is a highly dynamic phenomena consisting of a series of successive elementary heating and cooling episodes in the photosphere. These results agree with the recursive and continuous small-scale heating event in the photosphere found via high-resolution high cadence observations with the SST (Watanabe et al. 2011; Rutten et al. 2013).

Finally, we discuss why the small EB structure derived from the present multiline spectral analysis is in apparent contradiction to the tall flame-like EB structure found with the SST (Watanabe et al. 2011). We believe that the reason is due to projection effects. Our FISS observations, even being relatively closer to the disk center ($\mu=0.81$), still show a limb-ward extended $H\alpha$ wing intensity. This means that the projected height for smaller heliocentric angles may be consistent with

the 600–1200 km tall EB flame observed by the SST. Moreover, the limited time cadence of our observations may also play a role, in which case the H α wing intensity observed with FISS could correspond only to the root of the flame. Another critical factor is the morphological differences between the H α wing intensity and those at other wavelengths. As noted earlier, the H α wing intensity outstands other sources, and this is the main factor in the outcome of our spectral modeling with the hot enough temperature for the H α line and weak enough not to disturb other lines. More difficult to explain is the orientation of the $H\alpha$ wing intensity different from that of other sources. Its detailed explanation is yet to be made, but this morphological characteristic is undoubtedly against the 1D plane–parallel approximation built in the present spectral modeling and demands addressing 3D radiative transfer (e.g., Leenaarts & Carlsson 2009). We speculate that the H α intensity extended limb-ward represent hot particles ejected upright whereas the thermalized particles in the low photosphere dominate the Ca II 8542 Å wing and UV continuum sources. The morphological discrepancy will then result if the H α line remembers the nonequilibrium excitation for a longer time and the Ca II 8542 Å line quickly follows the thermal equilibrium. In this case, nonequilibrium $H\alpha$ opacity and hydrogen recombination can be essential to reproduce the observations. A proper account of such a time-dependent nonequilibrium effect is beyond the scope of this study. Since we have learned how to use the necessary numerical tools for computing EB-related spectral lines in this work, the next step we plan to take is to apply them to realistic simulations like those of Danilovic (2017) and Hansteen et al. (2017). The aim is to better understand the properties of EBs and to compare the synthetic spectra with those provided by high spatial resolution observations.

We greatly appreciate the anonymous referee for numerous suggestions that improved the manuscript to the present form. M.S. thanks Dr. T. M. D. Pereira for help with the RH code. M.S. and J.C. were supported by the Korea Astronomy and Space Science Institute for the R&D program, Development of a Solar Coronagraph on International Space Station (Project No. 2017-1-851-00), supervised by the Ministry of Science, ICT, and Future Planning, and by the National Research Foundation of Korea (NRF-2017 R1A2B4004466). J.L. is supported by the NNSFC grants 41331068, 11790303 (11790300), and 41774180. C.Q.N. acknowledges the support of the ISAS/JAXA International Top Young Fellowship (ITYF) and the JSPS KAKENHI grant No. 18K13596.

ORCID iDs

References

```
Bello González, N., Danilovic, S., & Kneer, F. 2013, A&A, 557, A102
Berlicki, A., & Heinzel, P. 2014, A&A, 567, A110
Berlicki, A., Heinzel, P., & Avrett, E. H. 2010, MmSAI, 81, 646
Bruls, J. H. M. J., Rutten, R. J., & Shchukina, N. G. 1992, A&A, 265, 237
Chae, J., Park, H.-M., Ahn, K., et al. 2013, SoPh, 288, 1
Danilovic, S. 2017, A&A, 601, A122
Eibe, M. T., Mein, P., Roudier, Th., & Faurobert, M. 2001, A&A, 371, 1128
Ellerman, F. 1917, ApJ, 46, 298
Fang, C., Tang, Y. H., Xu, Z., Ding, M. D., & Chen, P. F. 2006, ApJ,
  643, 1325
Fontenla, J., Avrett, E., & Loeser, R. 1993, ApJ, 406, 319
Georgoulis, M. K., Rust, D. M., Bernasconi, P. N., & Schmieder, B. 2002, ApJ,
Goode, P. R., Coulter, R., Gorceix, N., Yurchyshyn, V., & Cao, W. 2010, AN,
  331, 620
Grubecka, M., Schmieder, B., Berlicki, A., et al. 2016, A&A, 593, A32
Hansteen, V. H., Archontis, V., Pereira, T. M. D., et al. 2017, ApJ, 839, 22
Hashimoto, Y., Kitai, R., Ichimoto, K., et al. 2010, PASJ, 62, 879
Kitai, R. 1983, SoPh, 87, 135
Kurucz, R. L., & Bell, B. 1995, Atomic Line List (Cambridge, MA: Smithsonian
   Astrophysical Observatory) Kurucz CD-ROM No. 23
Landi Degl'Innocenti, E., & Landi Degl'Innocenti, M. 1977, A&A, 56, 111
Leenaarts, J., & Carlsson, M. 2009, in ASP Conf. Ser. 415, The Second Hinode
  Science Meeting: Beyond Discovery-Toward Understanding MULTI3D: A
  Domain-Decomposed 3D Radiative Transfer Code (San Francisco, CA:
Lemen, J. R., Title, A. M., Akin, D. J., et al. 2012, SoPh, 275, 17
Libbrecht, T., Joshi, J., Rodriguez, J. D. L. C., Leenaarts, J., & Ramos, A. A.
  2017, A&A, 598, A33
Matsumoto, T., Kitai, R., Shibata, K., et al. 2008, PASJ, 60, 577
Mein, P., & Rayrole, J. 1985, VA, 28, 567
Nelson, C. J., Doyle, J. G., Erdélyi, R., et al. 2013, SoPh, 283, 307
Qiu, J., Ding, M. D., Wang, H., Denker, C., & Goode, P. R. 2000, ApJL,
  544, L157
Quintero Noda, C., Shimizu, T., Rodriguez, J. D. L. C., et al. 2016, MNRAS,
  459, 3363
Quintero Noda, C., Uitenbroek, H., Carlsson, M., et al. 2018, MNRAS,
  481, 5675
Rutten, R. J. 2016, A&A, 590, A124
Rutten, R. J., Hammerschlag, R. H., & Bettonvil, F. M. 1997, ASSL, 225, 289
Rutten, R. J., Leenaarts, J., Rouppe van der Voort, L. H. M., et al. 2011, A&A,
  531, A17
Rutten, R. J., Rouppe van der Voort, L. H. M., & Vissers, G. J. M. 2015, ApJ,
  808, 133
Rutten, R. J., Vissers, G. J. M., Rouppe Van Der Voort, L. H. M.,
   Sütterlin, P., & Vitas, N. 2013, Journal of Physics: Conference Series, 440,
  012007
Scharmer, G. B., Bjelksjo, K., Korhonen, T. K., Lindberg, B., & Petterson, B.
  2003, Proc. SPIE, 4853, 341
Schou, J., Scherrer, P. H., Bush, R. I., et al. 2012, SoPh, 275, 229
Shine, R. A., & Linsky, J. L. 1974, SoPh, 39, 49
Socas-Navarro, H., Martinez Pillet, V., Elmore, D., et al. 2006, SoPh, 235, 75
Socas-Navarro, H., & Uitenbroek, H. 2004, ApJL, 603, L129
Uitenbroek, H. 2001, ApJ, 557, 389
Vernazza, J. E., Avrett, E. H., & Loeser, R. 1981, ApJS, 45, 635
Vissers, G. J. M., Rouppe Van Der Voort, L. H. M., & Rutten, R. J. 2013, ApJ,
  774, 32
Vissers, G. J. M., Rouppe van der Voort, L. H. M., Rutten, R. J.,
  Carlsson, M., & De Pontieu, B. 2015, ApJ, 812, 11
Watanabe, H., Vissers, G., Kitai, R., Rouppe van der Voort, L. H. M., &
  Rutten, R. J. 2011, ApJ, 736, 71
Yang, H., Chae, J., Lim, E.-K., et al. 2013, SoPh, 288, 39
Yang, H., Chae, J., Lim, E.-K., et al. 2016, ApJ, 829, 100
```